Fabrication of Copper Window Electrodes with ~10^8 Apertures cm^{-2} for Organic Photovoltaics

*H. Jessica Pereira[1], Joseph Reed[1], Jaemin Lee[1], Silvia Varagnolo[1], G. Dinesha. M. R. Dabera and Ross A. Hatton[1]**

[1] H. Jessica Pereira, Joseph Reed, Dr. Jaemin Lee, Dr. Silvia Varagnolo, Dr. G. Dinesha M. R. Dabera and Dr. R. A. Hatton

Department of Chemistry,

University of Warwick,

CV4 7AL, Coventry, United Kingdom

E-mail: (Ross.Hatton@warwick.ac.uk)

Abstract

We report a powerful approach to increasing the far-field transparency of copper film window electrodes which simultaneously reduces intra-band absorption losses for wavelengths < 550 nm and suppresses reflective losses for wavelengths > 550 nm. The approach is based on incorporation of a random array of ~100 million circular apertures per square cm into an optically thin copper film, with a mean aperture diameter of ~500 nm. A method for the fabrication of these electrodes is described that exploits a binary polymer blend mask that self-organises at room temperature from a single solution, and so is simple to

implement. Additionally all of the materials used in electrode fabrication are low cost, low toxicity and widely available. We show that these nano-structured copper electrodes offer an average far-field transparency of ≥ 80% and sheet resistance of ≤ 10 Ω sq^{-1} when used in conjunction with a conventional solution processed ZnO electron transport layer and demonstrate their utility in inverted organic photovoltaic devices.

Keywords: transparent electrode, copper, polymer blend lithography, solar cell, photovoltaic

Optically thin metal films with a thickness of < 10 nm are attracting growing attention as window electrodes for a variety of emerging applications[1–3] including thin film photovoltaics[4–6] and displays,[7,8] because they are compatible with flexible substrates[9–15] and can be deposited using simple vacuum evaporation. Roll-to-roll vacuum evaporation is attractive as a method for metal electrode deposition for organic optoelectronics[3,11] because it is a proven industrial process for the manufacture of low cost food packaging and insulation foils based on very thin metal films, offering excellent control over metal thickness and uniformity. Indeed for the large-scale manufacture of organic photovoltaics (OPVs) vacuum deposition of the metal electrode is expected to be

a tiny percentage of the total cost of a solution processed OPV.[16] To date, silver has been the metal of choice for window electrode applications[9,17] because it offers the highest electrical conductivity and lowest optical losses[18] over the visible and near infrared spectrum. To maximise transparency the thin silver film is typically sandwiched between two wide bandgap inorganic oxides or organic semiconductor layers to form a triple layer electrode architecture.[19] For price-sensitive applications such as OPVs copper is an attractive alternative to silver because it offers comparable electrical conductivity[18] at one hundredth of the cost.[20,21] To date there have been three recent reports of high performance OPVs, using a copper based window electrode that exhibits performance close to that achieved using an indium-tin oxide (ITO) electrode: Hutter *et al.* used an 8 nm thick thermally evaporated copper film and a WO_3 over layer which serves both as an anti-reflecting layer and hole-extraction layer.[22] Zhao *et al.*[23,24] have demonstrated a high performance window electrode based on a partially oxidised copper film sandwiched between ZnO layers, which proved to be remarkably stable towards air oxidation. However, in the latter case both the metal and oxide metal layers were deposited by the process of sputtering,[23,24] the slowness and complexity of which partially offsets the benefit of using a low-cost metal. A different approach for the passivation of optically thin copper film electrodes, that is compatible with vacuum evaporation, is the use of a sub-1 nm aluminium

over layer which also serves to reduce the electrode work function so that it can be used as the electron-extracting electrode in OPVs.[25]

For window electrode applications the primary disadvantage of copper as compared to silver is its lower far-field transparency for wavelengths below ~550 nm, which stems from intra-band absorptions[26,27] that do not occur in silver. For wavelengths above ~550 nm the transparency is reduced due to reflection similar to the case of silver. Ebner *et al*.[28] and Zhao *et al*.[24] have shown that absorption losses in optically thin copper films can be reduced to an acceptable level by reducing the thickness of the copper film, with a thickness of 6.5 nm proving to be most effective. Whilst losses due to reflection can be supressed using a wide band gap semi-conducing layer of specific thickness, there is a compromise to be struck between the optimal thickness to supress reflection and the thickness needed for optimal electronic functionality.

Herein we demonstrate a different approach to simultaneously reducing intra-band absorption losses in optically thin copper films for wavelengths below ~550 nm and dramatically suppressing reflection for wavelengths above ~550 nm, which is based on incorporating into the metal film ~100 million circular apertures per cm^2 with a mean diameter of ~ 500 nm. The size of the apertures is selected to be large enough to ensure that short wavelength light can pass through unhindered, whilst being small enough to ensure that, in the context of an OPV,

photo-generated free charge carriers formed in the light harvesting semiconductor adjacent to apertures in the metal electrode can still be extracted by the electrode without the need for a highly conducting charge extracting layer such as heavily doped poly(3,4-ethylenedioxythiophene) polystyrene sulfonate (PEDOT:PSS) to span the gaps in the electrode, as is the case for metal nanowire and metal grid electrodes.[29,30] This approach to metal window electrode design is applicable to thicker metal films than the optimal of 6.5 nm thickness reported previously,[24] which is likely to prove more practical to deposit over large areas. Conventional lithographic techniques for fabricating arrays of apertures of this size over large areas are prohibitively costly. One potentially low cost approach is to use micron-sized polymer nanoparticles as a shadow mask, deposited directly from a colloidal solution, which has been widely used[29,31–33], or formed by polymer blend lithography[34,35] followed by mask and metal lift-off. To our knowledge the work of Huang *et al.*[35] is the only literature pertaining to the use of polymer blend lithography as a mask to pattern metal films. Inspired by the latter, the electrode fabrication process reported herein is based on a simplified method of forming a dense array of apertures in metal films based on copolymer blend lithography that has the advantage that it does not require a metal lift-off step. We show that these electrodes are also easily combined with a widely used, solution processed, electron transport semiconductor that also serves as an anti-reflecting layer, to realise window electrodes suitable for use in OPVs. The

advantage of this approach to copper window electrode fabrication is the technological simplicity that results from the use of metal deposition by simple vacuum evaporation combined with a mask that self-organises from a single solution, instead of having to synthesise the mask prior to deposition onto the substrate to be etched, as is the case for conventional microsphere lithography. Also, all the solution-based steps use widely available low-cost chemicals, based on earth-abundant elements, and there is no requirement to control humidity or for post-deposition annealing of the polymer blend. When this electrode is used in conjunction with the solution processed wide bandgap *n*-type semiconductor ZnO, which is very widely used as an electron transport layer in OPVs, a dramatic ~66% reduction in electrode sheet resistance occurs due to low temperature diffusion of Cu into the adjacent ZnO layer, which greatly increases its performance as a transparent electrode for OPVs.

Results and Discussion

Figure 1 depicts the processes of electrode fabrication developed in this study. Copper films were thermally evaporated onto glass substrates modified with a mixed molecular layer of 3-mercaptopropyltrimethoxysilane (MPTMS) and 3-aminopropyltrimethoxysilane (APTMS). We have previously shown that this class of adhesion layer can be applied to both glass and plastic substrates to

realise robust copper films without contributing to light absorption.[29,36] A blend of the immiscible polymers, polystyrene (PS) and poly(methyl) methacrylate (PMMA) in 2-butanone was spin cast directly onto the copper film (Figure 1, step 1), whereupon spontaneous phase separation into well-defined isolated spherical PS domains in a PMMA matrix occurs. Crucially the PS domains protrude from the PMMA surface and extend through most, or all, of the film thickness. Selective removal of PS using cyclohexane (Figure 1, step 2) leaves behind a layer of PMMA with circular holes, which serves as a mask to etch copper. (Figure S1)

To date literature reports pertaining to phase separation in PS/PMMA blends have emphasised that the size of the PS domains in the PMMA matrix can be controlled by varying the polymer molecular mass combination,[34] or weight ratio,[35,37,38] or the humidity of the atmosphere in which the film is deposited[34], or with post-deposition annealing[38]. The deposition protocol reported herein is distinct from these earlier works in that the molecular mass and weight ratio of the two polymers is held constant and the PS domain size is controlled only by adjustment of the overall concentration of the polymer blend solution: A higher concentration yields larger PS domains suitable for transparent electrodes, whilst low concentrations give very small island sizes that couple strongly with incident light (Figure S2). Crucially this process does not require control over humidity or the need for post-deposition annealing, and so is more amenable to up-scaling.

An important step in the electrode fabrication processes is the brief UV/O_3 treatment to remove PMMA at the bottom of the holes formed by PS removal; Figure 1, step 3. PMMA is uniformly etched under exposure to UV radiation[39,40] and so this treatment ensures the holes in the PMMA film extend all the way through to the underlying copper film, as evidenced by the cross-sections of AFM images (Figure 2 and Figure S1(g)), forming a clear pathway for the etchant to travel to the surface of metal film. This step is necessary to achieve a high density and uniform distribution of holes in the copper film, without which a significant proportion of holes formed by removal of PS do not extend down to the underlying copper (Figure S1(f)).

Etching of the copper film through the PMMA mask (Figure 1, step 4) is achieved by dipping the substrate for 15-20 seconds into the low-cost etchant ammonium persulphate, which is a common oxidizing and bleaching agent. The etching process is very rapid because the metal thickness is very low, although it can be further speeded up by increasing the concentration of the etchant.

The PMMA mask is removed by ultra-sonic agitation in toluene, followed by glacial acetic acid. Glacial acetic acid simultaneously dissolves residual PMMA and any oxide layer at the surface of the copper film that may have formed if the etching processing is performed in air. Glacial acetic acid is known to preferentially remove copper oxides from the surface of copper leaving the

metal surface residue free[27,41]. Notably, for PMMA layers that are ≤ 25 nm thick acetic acid treatment alone is sufficient[41] to completely remove the PMMA layer. Together the process illustrated in Figure 1 enables the fabrication of copper electrodes with a random distribution of ~100 million circular apertures cm^{-2}, the average size of which can be altered by changing the concentration of the polymer blend, which enables control within the diameter range 50 to 1000 nm. (Figure S2)

For OPV device applications the sheet resistance of the window electrode is a key determinant of device performance and in practice cannot exceed 20 Ohms per square (Ω sq^{-1}) without incurring unacceptable electrical losses.[42–44] To determine the thickness needed to achieve the highest far-field transparency, whilst retaining a sheet resistance below 20 Ω sq^{-1}, different thicknesses of copper films ranging from 9 to 17 nm were used to fabricate electrodes with the same aperture size distribution shown in Figure 2(a). The total transmittance and reflectance (i.e. specular and scattered combined) is shown in Figure 3 for films with and without apertures. As expected the transmittance is highest for the thinnest film and the reflectance is greatest for the thickest film. The transmittance is increased by $\geq$ 20% in absolute terms when apertures are introduced into the film, across the wavelength range 400-850 nm. For wavelengths below ~ 550 nm the transmittance is increased by 20-25% for all metal thicknesses, which can be rationalised primarily in terms of a reduction in

absorption, since the aperture density and size distribution shown in Figure 2 corresponds to removal of one quarter (24 ± 1 %) of the metal electrode. For wavelengths above ~550 nm it is evident that the total reflectance is dramatically reduced upon incorporation of apertures, although this does not entirely translate into a commensurate increase in transparency. For example, for an 11 nm thick film the reflectance at 850 nm is reduced from ~45% to ~12%, a decrease of 33%, whilst the transparency increases from 50% to 75%; an increase of only 25%. The ~ 8% difference is attributed to parasitic absorption due to surface plasmon excitation in the copper electrode[14,45,46] which, as shown in the subsequent section, can be largely mitigated by appropriate selection of the adjacent charge transport layer.

The data in Figure 3 show that the highest transparency is achieved using the thinnest copper film. However, since sheet resistance increases with decreasing film thickness, as shown in Figure 4(a), a compromise must be struck between these properties for optimal performance as a window electrode in OPVs.[47] It is evident from Figure 4(a) that incorporation of apertures increases the sheet resistance for all metal thicknesses, consistent with scattering of electrons at the aperture edges.[29] The sheet resistance of films with apertures is only below 20 Ω sq^{-1} for a metal thickness above 14 nm. However, for application in OPVs the window electrode is invariably buried beneath a wide band gap

charge transport layer such as ZnO[48,49] or PEDOT:PSS[48], which both require annealing at low temperature (100-200°C) for optimal performance. In this study a solution processable ZnO electron extraction layer was used, which can be processed using a variety of deposition methods including screen printing and doctor blading. The ZnO annealing step was initially performed at 120 °C which, for an 11 nm thick copper film with apertures, resulted in a notable reduction in the sheet resistance of the electrode from 29.8 ± 0.7 Ω sq^{-1} to 24.2 ± 0.7 Ω sq^{-1}. Increasing the annealing temperature to 180 °C resulted in a larger reduction in sheet resistance to 17.9 ± 0.4 Ω sq^{-1}. Remarkably the sheet resistance continued to decrease upon long term storage in a glove box, reaching ~ 9.6 Ω sq^{-1} after 5 months storage. Over the same period there is a small reduction in the far-field transparency of ~ 2.6 % across the visible spectrum (Figure S3), although in terms of the electrode Haacke Figure of Merit (FoM)[50,51], which is widely used to compare the performance[8,19,23] of window materials, the benefit of the large reduction in sheet resistance far outweighs the detrimental effect of the small reduction in transparency: The FoM increases from from 0.0099 $Ω^{-1}$ to 0.0135 $Ω^{-1}$. To our knowledge, for a Cu based window electrode, this FoM has only been exceeded by electrodes with a more complex triple layer oxide-metal-oxide structure fabricated by sputtering deposition: Table S1. X-Ray diffraction analysis; Figure S4, reveals that this ~66% total reduction in sheet resistance cannot be attributed to a change in crystallinity of the copper film[14] since the

intensity of the reflections from Cu crystal planes does not change, consistent with the very high surface melting temperature of copper (>400°C)[52,53]. An alternative explanation is that the intrinsic conductivity of the ZnO film is increased when annealed at the higher temperature of 180 °C and/or the conductivity is increased due to doping of the ZnO by Cu that diffuses from the underlying Cu film. To test this hypothesis conductive atomic force microscopy (C-AFM) analysis was performed on nano-aperture Cu electrodes covered with a 62 nm thick ZnO overlayer annealed at 120 °C and 180 °C. It is evident from the C-AFM images and the corresponding cross-sections given in Figure 5, that the current drop across the aperture when annealed at 120 °C is very abrupt and distinct (indicated by green arrows), and so the boundary of the aperture in the underlying Cu layer is well-defined. Conversely, the electrode annealed at a higher temperature of 180 °C shows a more gradual drop in current as the probe moves over the site of an aperture in the underlying Cu film and has a minimum at the centre of the aperture, so the boundaries of the apertures appear more diffuse in the current map. These spatially resolved electrical measurements are compelling evidence for an increase in the conductivity of ZnO in the plane of the oxide close to the metal film, which is consistent with the reduction in measured sheet resistance. Notably however, the applied voltage for the electrode annealed at 180 °C is twice that needed to achieve the same current as compared to the film annealed at 120 °C (8V vs. 4V), which seems to contradict the

conclusion that the conductivity of the ZnO layer is increased in the sample annealed at 180 ºC. It is however important to note that C-AFM measures the conductance normal to the plane of the film surface, and so it is sensitive to variations in the conductivity of the uppermost surface of the oxide as compared to the bulk, which may have become more resistive due to a higher barriers to charge extraction/injection and transport at higher annealing temperature.[54]

Whilst solid state diffusion of Cu into the ZnO layer would be expected to be accelerated by thermal annealing, diffusion of Cu into oxides at very low temperature is also known,[22,55,56] and so electrical doping of the ZnO layer by Cu also offers an explanation for the reduction in electrode sheet resistance upon annealing. Direct evidence for Cu diffusion from the underlying Cu film into the ZnO layer is provided by XPS analysis of a Cu electrode buried beneath a 62 nm thick ZnO layer annealed at 120 ºC and 180 ºC: Figure S5 and Table S2. The escape depth of Cu 2p photoelectrons is limited to a less than 10 nm and so the presence of clearly defined Cu 2p peaks in the spectrum for the film annealed at 180 ºC, confirms that Cu has diffused through the entire thickness of the ZnO layer and the process is thermally accelerated. Based on this XPS analysis the elemental composition at the ZnO surface is estimated to be <1% Cu. Evidence for Cu-doping of the ZnO film at the sites above apertures in the Cu film is provided using spatially resolved Energy Dispersive X-ray spectroscopy (EDXS): Figure S6 and Table S3 although, unlike XPS, EDXS probes the

elemental composition of the entire ZnO thickness. It is clear from the composition derived from the EDXS analysis (Table S3) that the proportion of Cu in ZnO regions adjacent to the underlying Cu is very much higher than 1%, which evidences very extensive Cu diffusion into the ZnO overlayer. The large difference between the Cu concentration derived from XPS and EDXS measurements provides compelling evidence that the Cu concentration in the ZnO film normal to the plane of the film is not homogenous, but concentrated in the region nearest the Cu film. This gradient in Cu concentration offers a plausible explanation for the apparent reduction in conductivity of the ZnO film measured using C-AFM, since the conductivity of Cu doped ZnO is known to depend strongly on Cu concentration.[57,58] ZnO is known to exhibit *n*-type conductivity[59,60] and it has been shown that at low concentrations (< 1 %) Cu dopants act as deep acceptors, which reduce the *n*-type character by acting as a compensating center.[61] Conversely at higher concentrations of > 3% the conductivity is increased due to accumulation of metallic Cu at the grain boundaries, which reduces the contact resistance between the ZnO crystallites.[57] The high concentration of Cu dopant nearest the Cu film could therefore give rise to the observed reduction in the electrode sheet resistance. At the same time the low concentration of Cu dopant at the uppermost surface of the 62 nm ZnO film would reduce the *n*-type character of the oxide thus increasing the barrier to electron injection into the conduction band, which would manifest as an apparent

reduction in the conductivity normal to the plane of oxide film. To confirm that an increase in the conductivity of the ZnO overlayer is the reason for the reduction in the large electrode sheet resistance, the ZnO layer on 5 month old electrodes with a sheet resistance of 9 Ω sq^{-1} was selectively removed by etching with acetic acid: Figure S7.[27,41] After this treatment the sheet resistance increases to ~ 40 Ω sq^{-1}, which confirms that the doped ZnO overlayer is the reason for the reduction in sheet resistance. Notably, ~ 40 Ω sq^{-1} is ~ 10 Ω sq^{-1} higher than that of freshly etched Cu electrodes; 29.8 ± 0.7 Ω sq^{-1}. Such an increase is not however unexpected since: (i) The Cu that has diffused into the ZnO layer (and is thus removed upon etching) has reduced the thickness of the metal film.; (ii) At the interface between the Cu film and the ZnO overlayer it is plausible that the Cu has been partially oxidised, forming a thin Cu oxide interlayer which would be readily etched by acetic acid[27,41], and so this would also reduce the Cu metal thickness.

A Cu film thickness of 11 nm was chosen to demonstrate utility of this electrode and the window electrode in an OPV device. In OPVs the ZnO layer serves primarily as a charge extraction layer although, like other wide band gap charge extraction materials, can also serve as an anti-reflecting layer when used in conjunction with metal film window electrodes: Figure S8 shows how the transparency of an 11 nm copper film (without apertures) is improved as a function of the ZnO layer thickness (20 – 96 nm). The average transparency of

the copper electrode (400 – 800 nm) with apertures is increased from 75.9% to 84.1% using the optimised ZnO thickness of ~ 62 nm (Figure 4(b)), which is comparable to that achieved using thinner copper films without apertures reported previously (Table S1).[22–24,28]

Importantly, the inclusion of ZnO does not complicate the process of electrode fabrication, since wide band gap charge extraction layers are an essential component of high performance OPVs regardless of the choice of electrodes. To demonstrate these electrodes as window electrodes in OPVs, devices were fabricated with the architecture; Cu (11nm)/ZnO (*x* nm)/ PEI (2 nm) / PCE10 – $PC_{70}BM$ (160 nm) /MoO_3 (10 nm) / Ag (80 nm), where *x* = 20-62 nm. Whilst the highest electrode transmittance was achieved using a ZnO thickness of 62 nm, the efficiency of an OPV device depends on a complex interplay of optical and electrical factors,[53,62–64] and so devices with different thicknesses of ZnO ranging from 20-62 nm were tested: Table S3 and Figure S9. The device power conversion efficiency is maximised when the thickness of ZnO is 33 nm. Champion devices achieved a power conversion efficiency of 4.9% and 6.8% for devices using an 11 nm thick copper electrode without and with apertures respectively. The large difference in power conversion efficiency results from a ~35% improvement in short circuit current density (J_{sc}) in devices using the electrode with apertures, which is consistent with more light entering the device. Crucially, there is no significant difference in open-circuit voltage (V_{oc}) or device

fill-factor, which is consistent with the expectation that the apertures in the copper film electrode are sufficiently small not to require the use of a highly conducting polymer to span the apertures.

In summary, we have demonstrated a novel approach to simultaneously reducing intra-band absorption losses in optically thin copper films for wavelengths below ~550 nm and dramatically suppressing reflection for wavelengths above ~550 nm, which is based on incorporation of ~100 million circular apertures per cm^2 into the copper film with a mean aperture diameter of ~ 500 nm. Additionally, we have described a method for the realisation of such an electrode that could be applied to other thin metal films. The advantage of this method is that the mask self-organises at room temperature from a single solution, the metal is deposited by simple vacuum evaporation, and all subsequent steps are solution-based processes using widely available low-cost chemicals based on earth abundant elements, without the need to control humidity or for post-deposition annealing. Consequently, there is considerable potential for scaling of these electrodes for OPV applications. Remarkably, when this electrode is constrained beneath a solution processed ZnO layer, widely used as an electron transport layer in OPVs, brief thermal annealing at only 180 ^oC dramatically improves the electrode conductivity due to spontaneous diffusion of Cu into the ZnO over layer which is particularly important for improving the

conductivity across those regions above apertures in the Cu film, which ensures that the device fill-factor is not degraded as compared to that achieved using an electrode without apertures in the Cu film. Notably, in the current study the Cu electrodes are supported on glass for ease of handing. However, we have previously demonstrated that unpatterned optically thin Cu films of the same thickness have identical properties on glass and plastic substrates when using the metal deposition protocol used in the current work.[36] Since the approach reported herein for the formation of apertures in Cu films is compatible with plastic substrates, there is no barrier to translating this approach to plastic substrates for the realisation of flexible OPVs.

Methods

Substrate cleaning: Glass substrates of the required dimension (12×12 mm for OPV devices and 26 × 26 mm for electrode characterisation) were cut from 1.2 mm thick glass microscope slides (Academy) and 12 × 12 mm glass substrates with an 8 mm wide ITO strip were purchased from Thin Film Devices Inc. with an ITO stated thickness of 145 nm ± 10 nm and a sheet resistance of 15 Ω sq^{-1} ± 3 Ω sq^{-1}. Both types of substrates were cleaned by ultrasonic agitation in a diluted solution of surfactant, deionized water, acetone and IPA for 30 minutes each followed by drying with a stream of nitrogen and UV/O_3 treatment for 15 minutes.

Mixed Monolayer deposition: For glass substrates, a mixed monolayer was deposited prior to evaporation of Cu by exposing the substrates to vapors of 3-mercaptopropyltrimethoxysilane (MPTMS, Sigma Aldrich) and 3-aminopropyltrimethoxysilane (APTMS, Sigma Aldrich) at 50 mbar for 4 hours immediately after UV/O_3 treatment.

All electrode and device fabrication were carried out in a nitrogen filled glove box with a O_2 level < 1 ppm unless otherwise stated. Evaporation of metals and metal oxides were carried out with a CreaPhys Organic Molecular evaporator co-located in the same glove box. The thickness of deposited layers was monitored using a carefully calibrated quartz-crystal microbalance mounted adjacent to the substrate. All metals were thermally evaporated from tungsten boats. MoO_3 was thermally evaporated using boron nitride crucibles. The working pressure of the evaporator was $< 1\times10^{-5}$ mbar.

Deposition of copper: Cu was deposited by thermal evaporation of Cu pellets at a rate of 2.2 – 2.5 Å s^{-1} to give the required thickness.

Fabrication of apertures using polymer blend lithography: A polymer blend consisting of PS (Mw = 280 000) and PMMA (Mw = 50 000) in the weight ratio of 3:7 having a concentration of 15 mg ml^{-1} was prepared in 2-butanone. The blend was deposited on Cu by spin coating at 2500 rpm for 60 seconds. The PS entities were selectively removed by rinsing the films in cyclohexane followed

by UV/O_3 treatment for 15 minutes. A dilute solution of ammonium persulphate (0.002 mol dm^{-3}) was used to etch Cu through the PMMA mask to fabricate holes by immersing the substrates in the etchant for 15-20 seconds followed by drying with a stream of nitrogen. The PMMA template was finally removed by ultrasonic agitation in toluene and then in glacial acetic acid.

For the selective removal of the 62 nm ZnO layer from a 62 nm ZnO / 11 nm Cu film the sample was etched with glacial acetic acid for ~1 min.

Morphology and distribution of apertures: Atomic Force Microscope (AFM) imaging was performed using an Asylum Research MFP – 3D operated in tapping mode to study the morphology of the Cu films. The size distribution of apertures was evaluated using WXsM software. Conducting AFM (C-AFM) was performed on nano-aperture copper films with ZnO using the same instrument in contact mode by applying a constant voltage between the tip and the sample holder and the resulting morphology and current maps were analyzed using the Asylum Research AFM software. Scanning electron microscopy (SEM) imaging was performed using ZEISS Gemini 500 with an accelerating voltage of typically 0.3-0.6 kV to evaluate the distribution and coverage of apertures. Energy Dispersive X-ray spectroscopy (EDXS) spectra were recorded using an Oxford Instruments Si-Li detector unit on the SEM instrument, at an accelerating voltage of 17 keV.

Optical Transparency and Reflectance measurements: Far-field transmittance and reflectance of metal films on glass were measured over the wavelength range of 350 – 850 nm using 150 mm Spectralon® Integrating Sphere coupled to PerkinElmer® LAMBDA™ high performance series of UV/Vis spectrometer. The incident beam passed through the substrate first.

X-ray Diffraction Measurements: X-ray diffraction (XRD) measurements were carried out using a Siemens D5000 X-ray diffractometer operated in grazing angle using Cu (Kα) radiation with a wavelength of 1.542 Å. The scans were run for 14 h (for better peak resolution) and the samples (on glass) were mounted inside a purged graphite dome under a continuous flow of N_2 to avoid formation of copper oxides during prolonged scans. The XRD peaks were assigned using the Mercury software and the CDS National Chemical Database.

X-ray Photoelectron Spectroscopy measurements: XPS measurements were performed using a Kratos Axis Ultra DLD spectrometer. The samples were illuminated using X-rays from a monochromated Al Kα source (hν=1486.6 eV) and detected at a take-off angle of 90°. The resolution, binding energy referencing, and transmission function of the analyser were determined using a clean polycrystalline Ag foil. XPS peak fitting was carried out using the CasaXPS software (Voigt-mixed Gaussian−Lorentzian line shapes and a Shirley

background). The peaks were corrected with respect to C1s at 284.7 eV due to the use of neutraliser to avoid charging.

Fabrication of OPV devices: A ZnO ink (5.6% w/v) in IPA was purchased from Infinity PV and a diluted solution (0.5% w/v – 1.4% w/v) was spun at 1000 rpm for 60 seconds followed by annealing at 180 ^{o}C for 15 minutes to fabricate the ETL. The enhanced device performance obtained by incorporating an ultra-thin layer of poly(ethyleneimine) (PEI) or poly-(ethyleneimine)-ethoxylated (PEIE) has already been reported[53,62,63]. Therefore, a thin layer of PEI was spun on top of ZnO as a capping layer[53], following the annealing process to maximize device performance. PCE10 (Poly[4,8-bis(5-(2-ethylhexyl)thiophen-2-yl)benzo[1,2-b;4,5-b']dithiophene-2,6-diyl-alt-(4-(2-ethylhexyl)-3-fluorothieno[3,4-b]thiophene-)-2-carboxylate-2-6-diyl)]) and $PC_{70}BM$ ([6,6]-Phenyl-C_{71}-butyric acid methyl ester) were mixed in 2:3 mass ratio to make a 35 mg ml^{-1} solution in chlorobenzene (97%) and 1,8-diiodooctane (3%) and deposited by spin coating from a static start at 3000 rpm for 120 seconds to form the photoactive layer. These slides were left inside the evaporator overnight and MoO_3 (10 nm at 0.1-0.2 Å s^{-1}) was deposited as the HTL followed by Ag (80 nm at 1.0-1.2 Å s^{-1}). Notably, whilst the molybdenum oxide layer is deposited from a powder of MoO_3, it is known that during vacuum evaporation it is expected to be partially reduced to MoO_{3-x} where x is < 0.3. Ag was deposited through a shadow mask to give an electrode area of 0.06 cm^2.

Characterization of OPV devices: Current density-voltage (*JV*) testing was performed in the dark and under 1 sun simulated solar illumination using a Keithley 2400 source measurement unit (SMU) and a custom Labview interface using an ABET technologies Sun 2000 Solar Simulator. The intensity was set to 100 mW cm^{-2} over the AM 1.5 solar spectrum. The light source was calibrated using a calibrated silicon diode. OPV devices were measured through a mask having a pixel area of 0.013 cm^2. EQE measurements were done using a white light xenon arc lamp (Sciencetech SF150), monochromator (Photon Technology International), focusing and splitting lenses, current-voltage amplifier (Femto DHPCA-100), lock-in amplifier (Stanford Research SR830 DSP) and a custom Labview interface.

Acknowledgements

The authors would like to thank the United Kingdom Engineering and Physical Sciences Research Council (EPSRC) for funding (Grant number: EP/N009096/1) and the University of Warwick for the award of a Chancellor's International Scholarship to H. Jessica Pereira.

Data Availability

All data supporting this study are provided as supplementary information accompanying this paper.

References

[1] S. Lam Po Tang, *Trans. Inst. Meas. Control* **2007**, *29*, 283.

[2] Z. Yang, J. Deng, X. Sun, H. Li, H. Peng, *Adv. Mater.* **2014**, *26*, 2643.

[3] J. Yun, *Adv. Funct. Mater.* **2017**, *27*.

[4] Q. Wang, Y. Xie, F. Soltani-Kordshuli, M. Eslamian, Progress in emerging solution-processed thin film solar cells - Part I: Polymer solar cells. *Renew. Sustain. Energy Rev.* **2016**, *56*, 347–361.

[5] B. Kippelen, J.-L. Bredas, *Energ Env. Sci* **2009**, *2*, 251.

[6] Z. Tang, W. Tress, O. Ingan??s, Light trapping in thin film organic solar cells. *Mater. Today* **2014**, *17*, 389–396.

[7] J. Lee, P. Lee, H. Lee, D. Lee, S. S. Lee, S. H. Ko, *Nanoscale* **2012**, *4*, 6408.

[8] A. R. Madaria, A. Kumar, C. Zhou, *Nanotechnology* **2011**, *22*.

[9] J. Zou, C. Z. Li, C. Y. Chang, H. L. Yip, A. K. Y. Jen, *Adv. Mater.* **2014**, *26*, 3618.

[10] M. Kaltenbrunner, M. S. White, E. D. Głowacki, T. Sekitani, T. Someya, N. S. Sariciftci, S. Bauer, *Nat. Commun.* **2012**, *3*, 770.

[11] D. S. Ghosh, Springer, Heidelberg, 2013; pp. 11–32.

[12] M. Pagliaro, G. Palmisano, R. Ciriminna, *Flex. Sol. Cells* **2008**, 1.

[13] W. S. Wong, A. Salleo, *Flexible electronics : materials and applications*; Springer, 2008.

[14] H. J. Pereira, O. S. Hutter, G. D. M. R. Dabera, L. A. Rochford, R. A. Hatton, *Sustain. Energy Fuels* **2017**, *1*, 859.

[15] R. D. I. G. Dharmasena, K. D. G. I. Jayawardena, C. A. Mills, J. H. B. Deane, J. V. Anguita, R. A. Dorey, S. R. P. Silva, *Energy Environ. Sci.* **2017**, *10*, 1801.

[16] C. J. Mulligan, M. Wilson, G. Bryant, B. Vaughan, X. Zhou, W. J. Belcher, P. C. Dastoor, *Sol. Energy Mater. Sol. Cells* **2014**, *120*, 9.

[17] A. Kim, Y. Won, K. Woo, C. H. Kim, J. Moon, *ACS Nano* **2013**, *7*, 1081.

[18] P. R. West, S. Ishii, G. V. Naik, N. K. Emani, V. M. Shalaev, A. Boltasseva, *Laser Photonics Rev.* **2010**, *4*, 795.

[19] L. Peres, A. Bou, D. Barakel, P. Torchio, *RSC Adv.* **2016**, *6*, 61057.

[20] A. R. Rathmell, S. M. Bergin, Y. L. Hua, Z. Y. Li, B. J. Wiley, *Adv. Mater.* **2010**, *22*, 3558.

[21] U.S.Geological Survey, *Mineral Commodity Summaries*; 2016.

[22] O. S. Hutter, R. A. Hatton, *Adv. Mater.* **2015**, *27*, 326.

[23] G. Zhao, W. Wang, T. S. Bae, S. G. Lee, C. W. Mun, S. Lee, H. Yu, G. H. Lee, M. Song, J. Yun, *Nat. Commun.* **2015**, *6*, 8830.

[24] G. Zhao, M. Song, H. S. Chung, S. M. Kim, S. G. Lee, J. S. Bae, T. S. Bae, D. Kim, G. H. Lee, S. Z. Han, H. S. Lee, E. A. Choi, J. Yun, *ACS Appl. Mater. Interfaces* **2017**, *9*, 38695.

[25] O. S. Hutter, H. M. Stec, R. A. Hatton, *Adv. Mater.* **2013**, *25*, 284.

[26] C. Gong, M. S. Leite, *ACS Photonics* **2016**, *3*, 507.

[27] G. H. Chan, J. Zhao, E. M. Hicks, G. C. Schatz, R. P. Van Duyne, *Nano Lett.* **2007**, *7*, 1947.

[28] D. Ebner, M. Bauch, T. Dimopoulos, *Opt. Express* **2017**, *25*, A240.

[29] H. M. Stec, R. J. Williams, T. S. Jones, R. A. Hatton, *Adv. Funct. Mater.* **2011**, *21*, 1709.

[30] J. E. Lim, S. M. Lee, S. S. Kim, T. W. Kim, H. W. Koo, H. K. Kim, *Sci. Rep.* **2017**, *7*, 1.

[31] N. Kwon, K. Kim, S. Sung, I. Yi, I. Chung, *Nanotechnology* **2013**, *24*.

[32] T. Gao, B. Wang, B. Ding, J. Lee, P. W. Leu, *Nano Lett.* **2014**, 2105.

[33] P. Colson, C. Henrist, R. Cloots, *J. Nanomater.* **2013**, *2013*.

[34] C. Huang, M. Moosmann, J. Jin, T. Heiler, S. Walheim, T. Schimmel,

Beilstein J. Nanotechnol. **2012**, *3*, 620.

[35] C. Huang, A. Förste, S. Walheim, T. Schimmel, *Beilstein J. Nanotechnol.* **2015**, *6*, 1205.

[36] H. M. Stec, R. A. Hatton, *ACS Appl. Mater. Interfaces* **2012**, *4*, 6013.

[37] I. Prosycevas, S. Tamulevicius, A. Guobiene, *Thin Solid Films* **2004**, *453–454*, 304.

[38] D. U. Ahn, Z. Wang, I. P. Campbell, M. P. Stoykovich, Y. Ding, *Polym. (United Kingdom)* **2012**, *53*, 4187.

[39] S. Eve, J. Mohr, *Procedia Eng.* **2009**, *1*, 237.

[40] C. Wochnowski, M. A. S. Eldin, S. Metev, *Polym. Degrad. Stab.* **2005**, *89*, 252.

[41] K. L. Chavez, D. W. Hess, *J. Electrochem. Soc.* **2003**, *150*, G284.

[42] S. Choi, W. J. Potscavage, B. Kippelen, *J. Appl. Phys.* **2009**, *106*.

[43] J.-W. Kang, S.-P. Lee, D.-G. Kim, S. Lee, G.-H. Lee, J.-K. Kim, S.-Y. Park, J. H. Kim, H.-K. Kim, Y.-S. Jeong, *Electrochem. Solid-State Lett.* **2009**, *12*, H64.

[44] H. Jin, A. Pivrikas, K. H. Lee, M. Aljada, M. Hambsch, P. L. Burn, P. Meredith, *Adv. Energy Mater.* **2012**, *2*, 1338.

[45] M. Schwind, B. Kasemo, I. Zorić, *Nano Lett.* **2013**, *13*, 1743.

[46] T. H. Park, N. Mirin, J. B. Lassiter, C. L. Nehl, N. J. Halas, P. Nordlander, *ACS Nano* **2008**, *2*, 25.

[47] B. O'Connor, C. Haughn, K. H. An, K. P. Pipe, M. Shtein, *Appl. Phys. Lett.* **2008**, *93*, 1.

[48] L. Lu, T. Zheng, Q. Wu, A. M. Schneider, D. Zhao, L. Yu, *Chem. Rev.* **2015**, *115*, 12666.

[49] B. Xiao, H. Wu, Y. Cao, *Mater. Today* **2015**, *18*, 385.

[50] G. Haacke, *J. Appl. Phys.* **1976**, *47*, 4086.

[51] G. Haacke, *Annu. Rev. Mater. Sci.* **1977**, *7*, 73.

[52] G. Y. Krasnikov, V. P. Bokarev, *J. Surf. Investig. X-ray, Synchrotron Neutron Tech.* **2015**, *9*, 1116.

[53] S. Woo, W. Hyun Kim, H. Kim, Y. Yi, H. K. Lyu, Y. Kim, *Adv. Energy Mater.* **2014**, *4*, 1.

[54] M. Krzywiecki, L. Grządziel, A. Sarfraz, D. Iqbal, A. Szwajca, A. Erbe, *Phys. Chem. Chem. Phys.* **2015**, *17*, 10004.

[55] M. T. Greiner, L. Chai, M. G. Helander, W. M. Tang, Z. H. Lu, *Adv. Funct. Mater.* **2013**, *23*, 215.

[56] D.-T. Nguyen, S. Vedraine, L. Cattin, P. Torchio, M. Morsli, F. Flory, J. C. Bernède, *J. Appl. Phys.* **2012**, *112*, 63505.

[57] P. Samarasekara, U. Wijesinghe, E. N. Jayaweera, *GESJ Phys.* **2015**, *1*, 3.

[58] A. S. Yusof, Z. Hassan, N. Zainal, *Mater. Res. Bull.* **2018**, *97*, 314.

[59] A. Janotti, C. G. Van De Walle, *Reports Prog. Phys.* **2009**, *72*.

[60] K. Tang, S.-L. Gu, J.-D. Ye, S.-M. Zhu, R. Zhang, Y.-D. Zheng, *Chinese Phys. B* **2017**, *26*, 47702.

[61] G. Muller, *Phys. Status Solidi* **1976**, *76*, 525.

[62] H. Kim, S. Nam, J. Jeong, S. Lee, J. Seo, H. Han, Y. Kim, *Korean J. Chem. Eng.* **2014**, *31*, 1095.

[63] Z. He, H. Wu, Y. Cao, *Adv. Mater.* **2014**, *26*, 1006.

[64] T. Karabacak, J. S. Deluca, P. I. Wang, G. A. Ten Eyck, D. Ye, G. C. Wang, T. M. Lu, *J. Appl. Phys.* **2006**, *99*, 1.

[65] X. Wang, R. Wang, H. Zhai, X. Shen, T. Wang, L. Shi, R. Yu, J. Sun, *ACS Appl. Mater. Interfaces* **2016**, *8*, 28831.

[66] C. Sachse, N. Weiß, N. Gaponik, L. Müller-Meskamp, A. Eychmüller, K. Leo, *Adv. Energy Mater.* **2014**, *4*, 1.

[67] A. R. Rathmell, B. J. Wiley, *Adv. Mater.* **2011**, *23*, 4798.

[68] J. Song, J. Li, J. Xu, H. Zeng, *Nano Lett.* **2014**, *14*, 6298.

Figures

Figure – Table of Contents

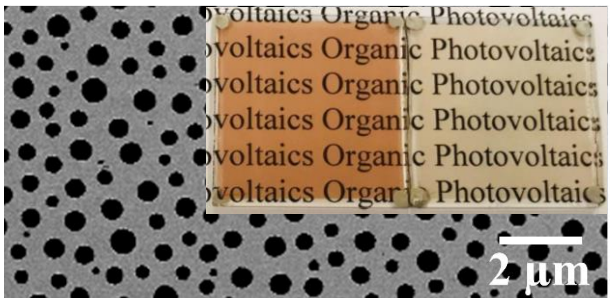

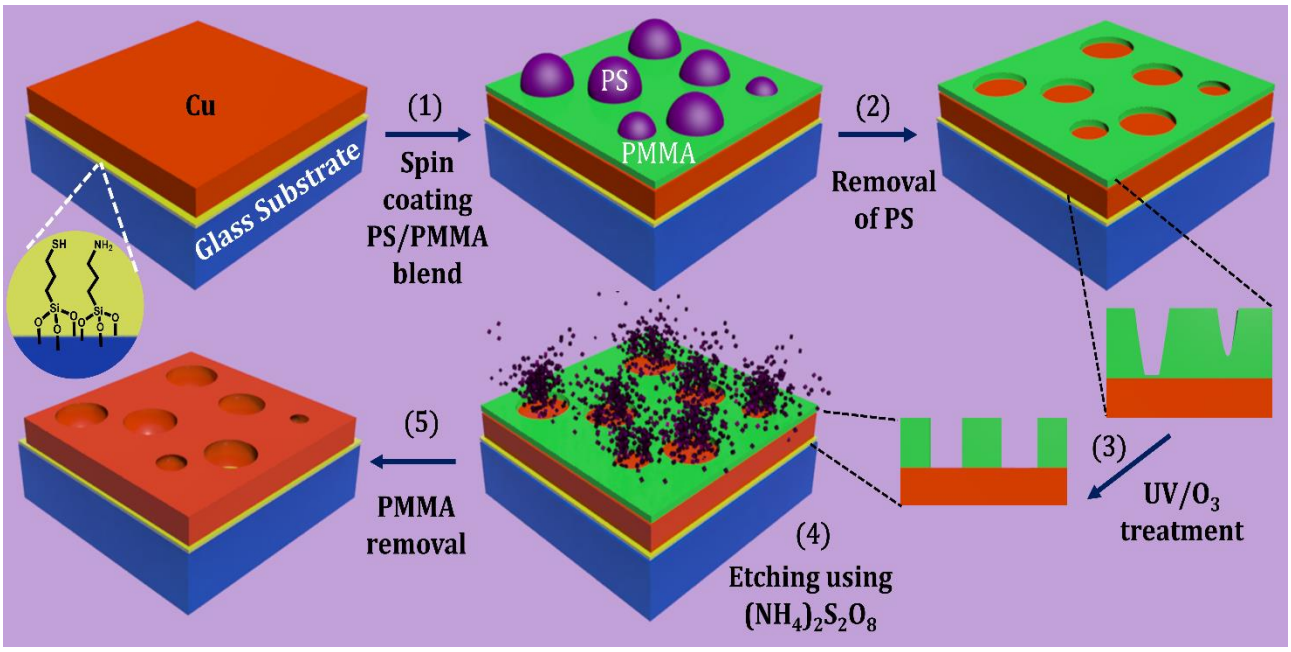

Figure 1: Schematic of electrode fabrication process.

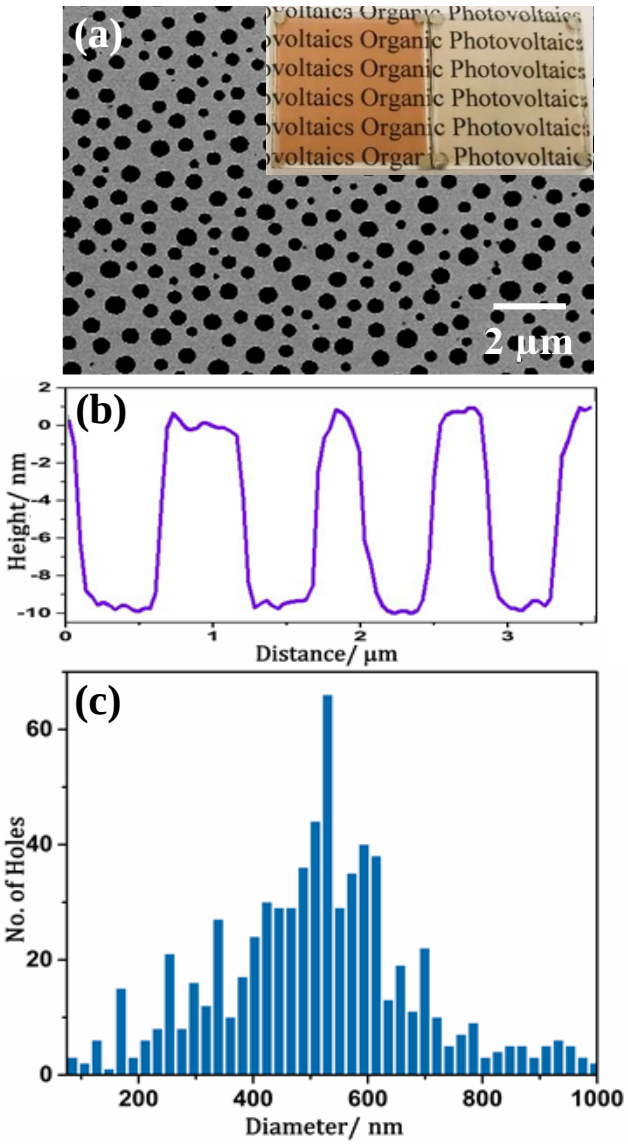

Figure 2: (a) SEM showing the morphology of 11 nm thick copper films with apertures; **Inset:** A photograph of an 11 nm thick copper electrode with (right) and without (left) apertures; **(b)** cross-section taken from an AFM image of the same sample as in (a) showing the depth of the apertures; and **(c)** histogram showing the size distribution of apertures computed for a 20 × 20 μm^2 AFM image.

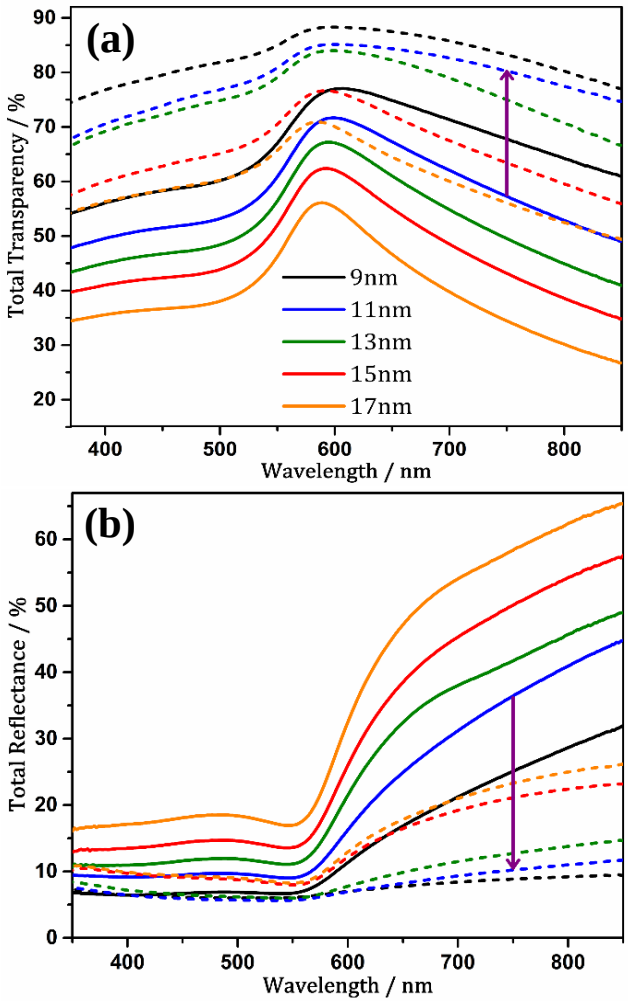

Figure 3: (a) Total far-field transparency and; **(b)** reflectance of different thicknesses of Cu films (referenced to glass) with (broken lines) and without (solid lines) apertures.

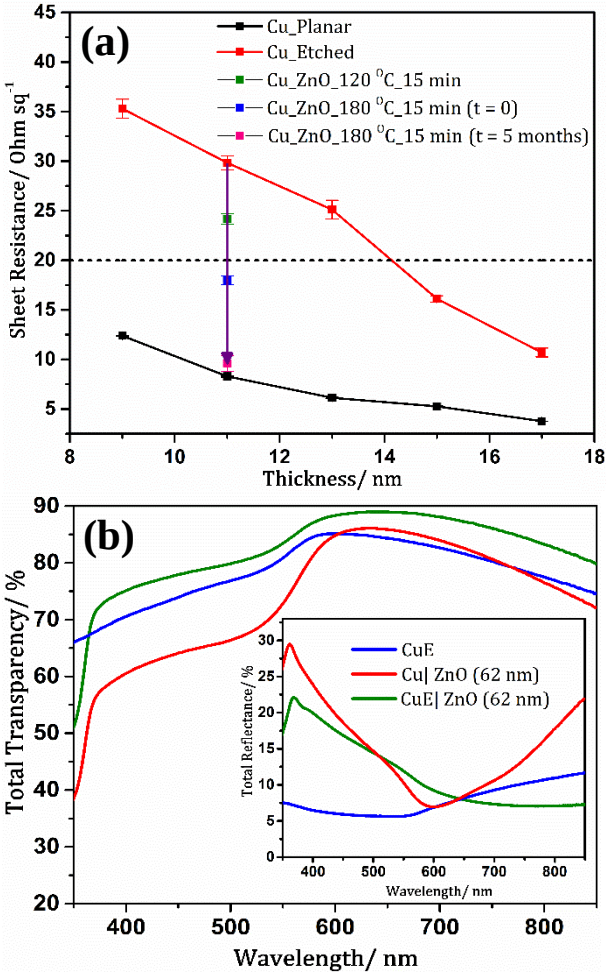

Figure 4: **(a)** Sheet resistance as a function of thickness for electrodes of different thicknesses with (red) and without (black) apertures, and the change in sheet resistance when 11 nm films are annealed at 120 ºC and 180 ºC (t = 0 and t = 5 months) following deposition of a 62 nm ZnO over layer ; **(b)** Total far-field transparency (referenced to glass) and; **inset:** total reflectance for 11 nm copper film with apertures (CuE) and copper film with 62 nm ZnO over layer with and without apertures.

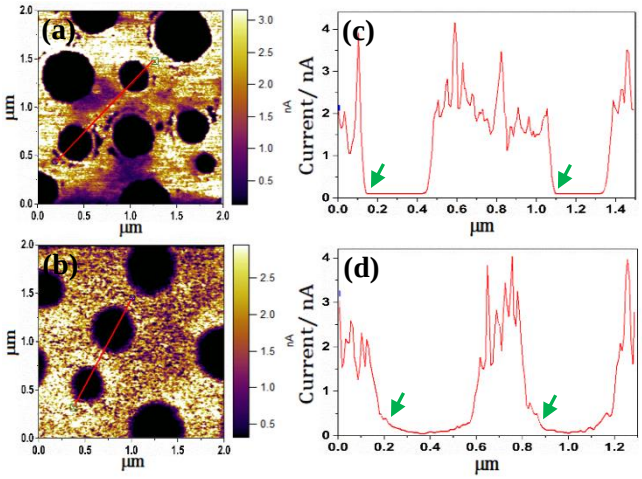

Figure 5: C-AFM images showing the current profiles obtained by applying a bias of 4V and 8V respectively for Cu nanohole electrodes with 62 nm ZnO annealed at **(a)**120 ºC and **(b)**180 ºC; **(c)** and **(d)** correspond to the cross sections of (a) and (b) respectively along the lines shown.

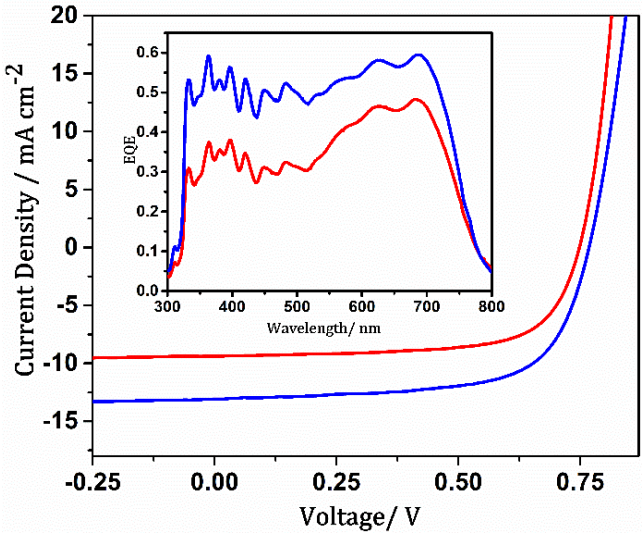

Figure 6: Representative current density-voltage and; **Inset:** external quantum efficiency data recorded under one sun simulated solar illumination (100 mW cm^{-2}; AM 1.5G) for devices with the architecture: Cu (11nm) with (blue) and without (red) apertures/ ZnO (33 nm)/ PEI (2 nm) / PCE10 – $PC_{70}BM$ (160 nm)

/MoO_3 (10 nm) / Ag (80 nm). The integrated EQE for the red and blue curves shown are 9.17 mA cm^{-2} and 12.30 mA cm^{-2} respectively which is within 3.7% of the measured J_{sc}.

Supporting Information

Fabrication of Copper Window Electrodes with ~10^8 Apertures cm^{-2} for Organic Photovoltaics

*H. Jessica Pereira[1], Joseph Reed[1], Jaemin Lee[1], Silvia Varagnolo[1], G. Dinesha. M. R. Dabera and Ross A. Hatton[1]**

[1] H. Jessica Pereira, Joseph Reed, Dr. Jaemin Lee, Dr. Silvia Varagnolo, Dr. G. Dinesha M. R. Dabera and Dr. R. A. Hatton

Department of Chemistry,

University of Warwick,

CV4 7AL, Coventry, United Kingdom

E-mail: (Ross.Hatton@warwick.ac.uk)

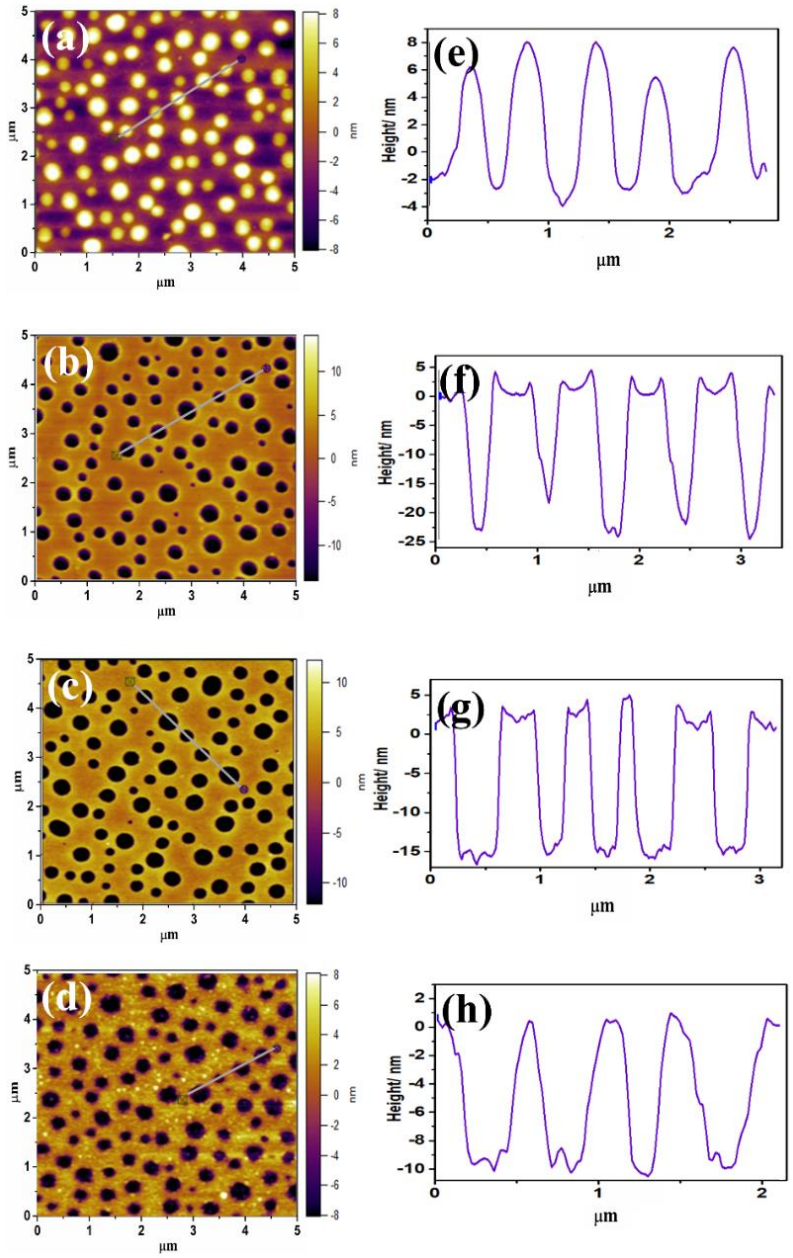

Figure S1: Atomic Force Microscopy (AFM) images showing the morphology of: **(a)** the PS:PMMA polymer blend (7.5 mg ml^{-1}) spin cast onto a copper film showing spherical PS islands dispersed in a PMMA matrix; **(b)** holes formed in the PMMA by selective removal of PS using cyclohexane; **(c)** UV/O_3 treated PMMA film on copper; **(d)** etched copper film showing circular apertures; **(e) – (h)** are representative AFM cross-sections taken from (a) – (d) respectively along

the lines shown. **(g)** shows that the holes in the PMMA layer extend to an equal depth after UV/O_3 treatment.

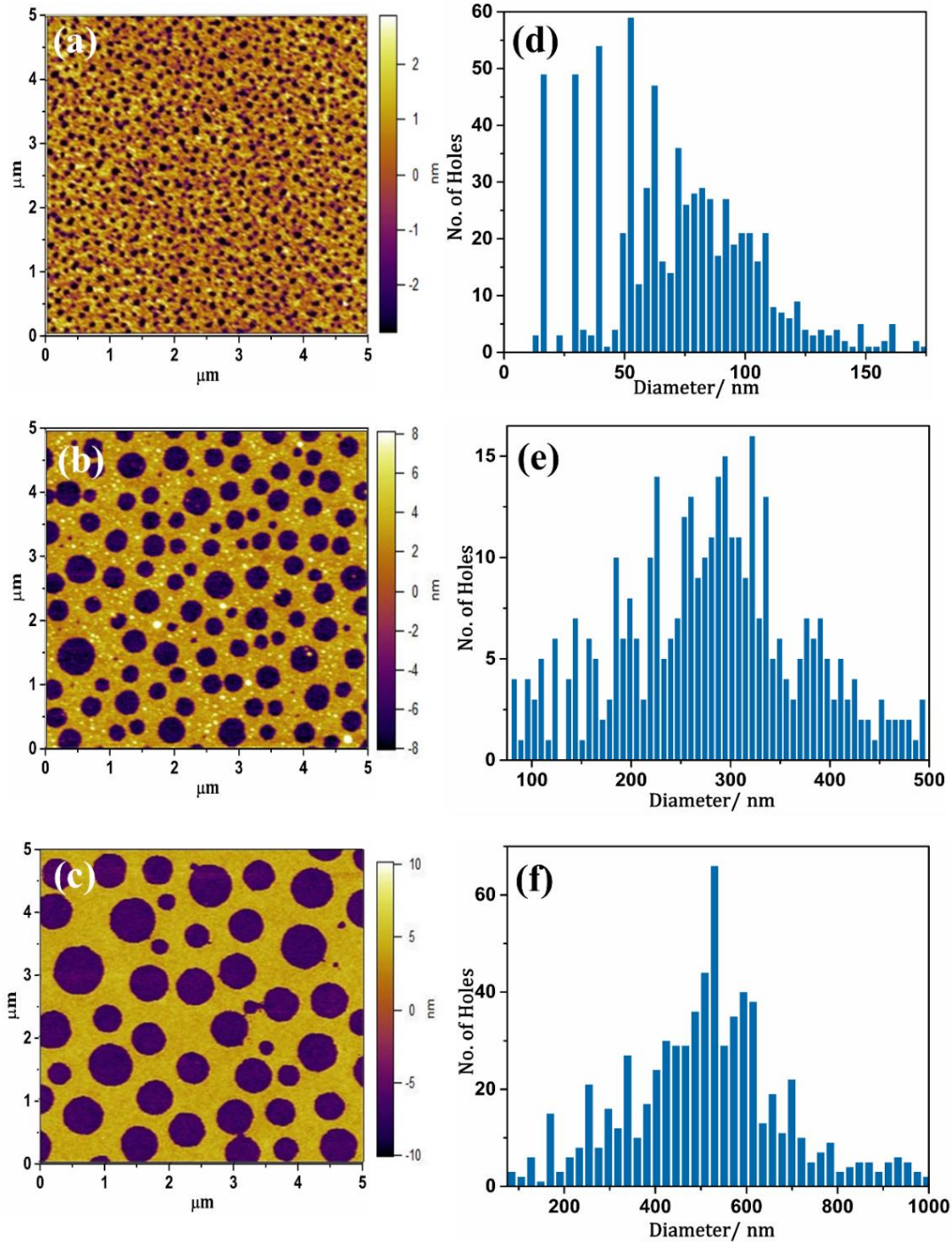

Figure S2: AFM images of copper electrodes (11 nm) etched using polymer blend solutions having concentrations **(a)** 0.28 mg ml^{-1}; **(b)** 7.5 mg ml^{-1}; **(c)** 15

mg ml^{-1} respectively; **(d)** size distribution of (a); **(e)** size distribution for (b) computed for a 10 × 10 μm^2 AFM image and **(f)** size distribution for (c) computed for a 20 × 20 μm^2 AFM image.

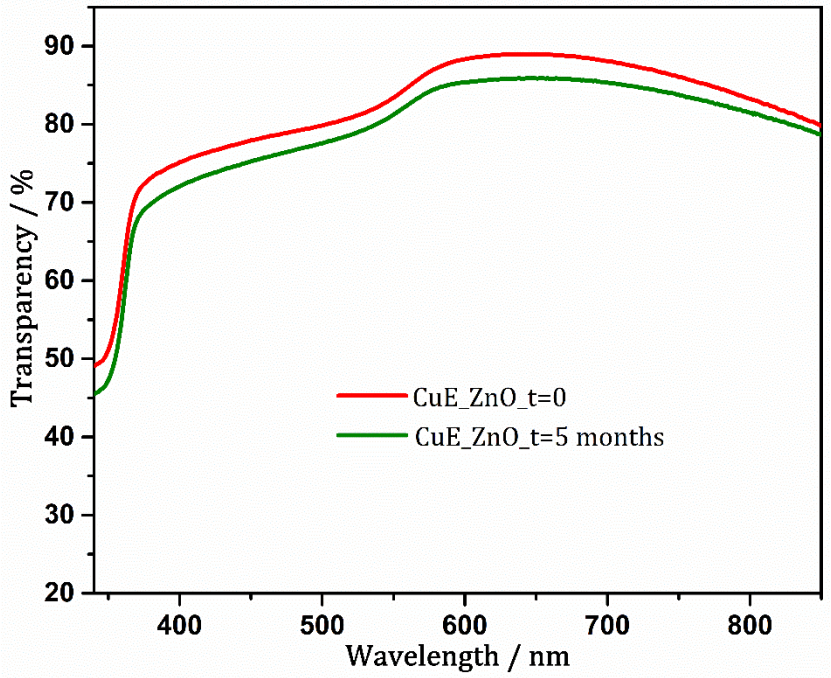

Figure S3: (a) Total far-field transparency of nano-aperture Cu electrodes (11nm) with ZnO (62 nm) annealed at 180 °C for 15 mins at t = 0 and t = 5 months.

Group	Substrate	Electrode Architecture	Average Transparency (T_{avg})	Sheet Resistance (Ω sq^{-1})	$\frac{T_{avg}^{10}}{R_{sh}}$ (Ω^{-1})
Zhao *et al.*[23,24]	PET	ZnO/Cu (9.5nm)/ZnO	79.47	9.49	0.0106
		ZnO/Cu (6.5nm) on Cu(O)/ZnO	85.84	11.12	0.0195
		ZnO/Cu (9.5nm) on Cu(O)/ZnO	83.54	6.26	0.0264
		ZnO/Cu (7 nm) (O = 5%) /ZnO	85	13	0.0151
		ZnO/Cu (8 nm) (O = 5%) /ZnO	83	9	0.0172
Wang *et al.*[65]	Glass/Polymer	Ag nanoparticle coated CuNWs	89.1	47	0.0067
Sachse *et al*.[66]	Glass	CuNWs	88	24	0.0116
Rathmell *et al.*[20][67]	Glass	CuNWs	65	15	0.0009
	Plastic	CuNWs	85	30	0.0066
Ebner *et al.*[28]	Glass	TiOx/Cu (10 nm)/AZO	80	6.5	0.0165
		TiOx/Cu (7.5 nm)/AZO	74	17	0.0029
Song *et al.*[68]	Glass/PET	CuNW films	80	26.2	0.0041
		CuNW elastomers	80	58.6	0.0018
Current Study	Glass	Cu(11nm) nano-aperture	79.1	29.8	0.0032
		Cu(11nm) nano-aperture/ZnO(t=0)	84.1	17.9	0.0099
		Cu(11nm) nano-aperture/ZnO(t=5 months)	81.5	9.6	0.0135

Table S1: Comparison of optical and electrical characteristics of different types of Cu electrodes reported. T_{avg} is the average far-field transparency between λ = 400-800 nm.

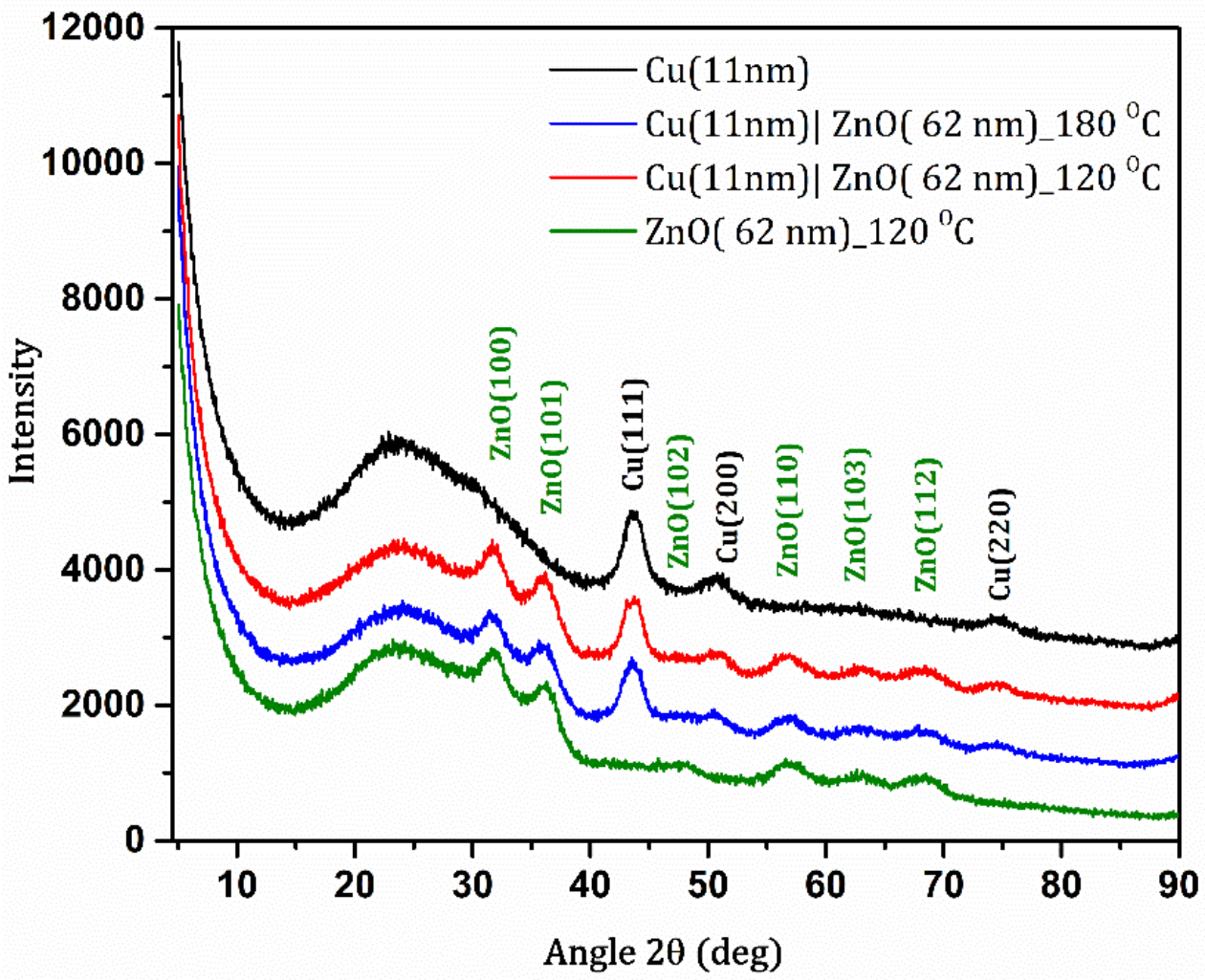

Figure S4: XRD pattern of Cu, ZnO annealed at 120°C, Cu/ZnO annealed at 120°C and 180°C. All films were deposited on glass and spectra have been offset along the *y*-axis for clarity. The XRD spectra for Cu and ZnO have been compared with the standards ICSD-43493 and ICSD-67454 respectively to assign peak positions.

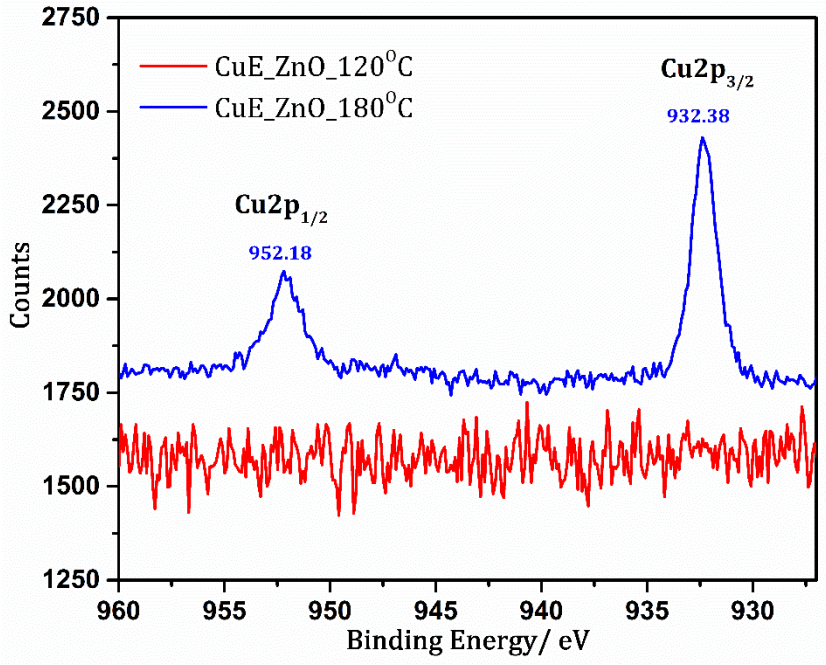

Figure S5: XPS spectra of nano-aperture Cu films with ZnO annealed at 120 ºC and 180 ºC on glass substrates showing the presence of Cu by the characteristic Cu $2p_{1/2}$ and Cu $2p_{3/2}$ peaks in the latter.

Element	**O**	**C**	**Cu**	**Zn**
Annealing Temperature - 120 ºC				
Percentage	48.7	30.2	0	21.1
Annealing Temperature - 180 ºC				
Percentage	45.8	37.3	0.86	16.0

Table S2: Elemental composition from XPS spectra of nano-aperture Cu films with ZnO annealed at 120 ºC and 180 ºC on glass substrates.

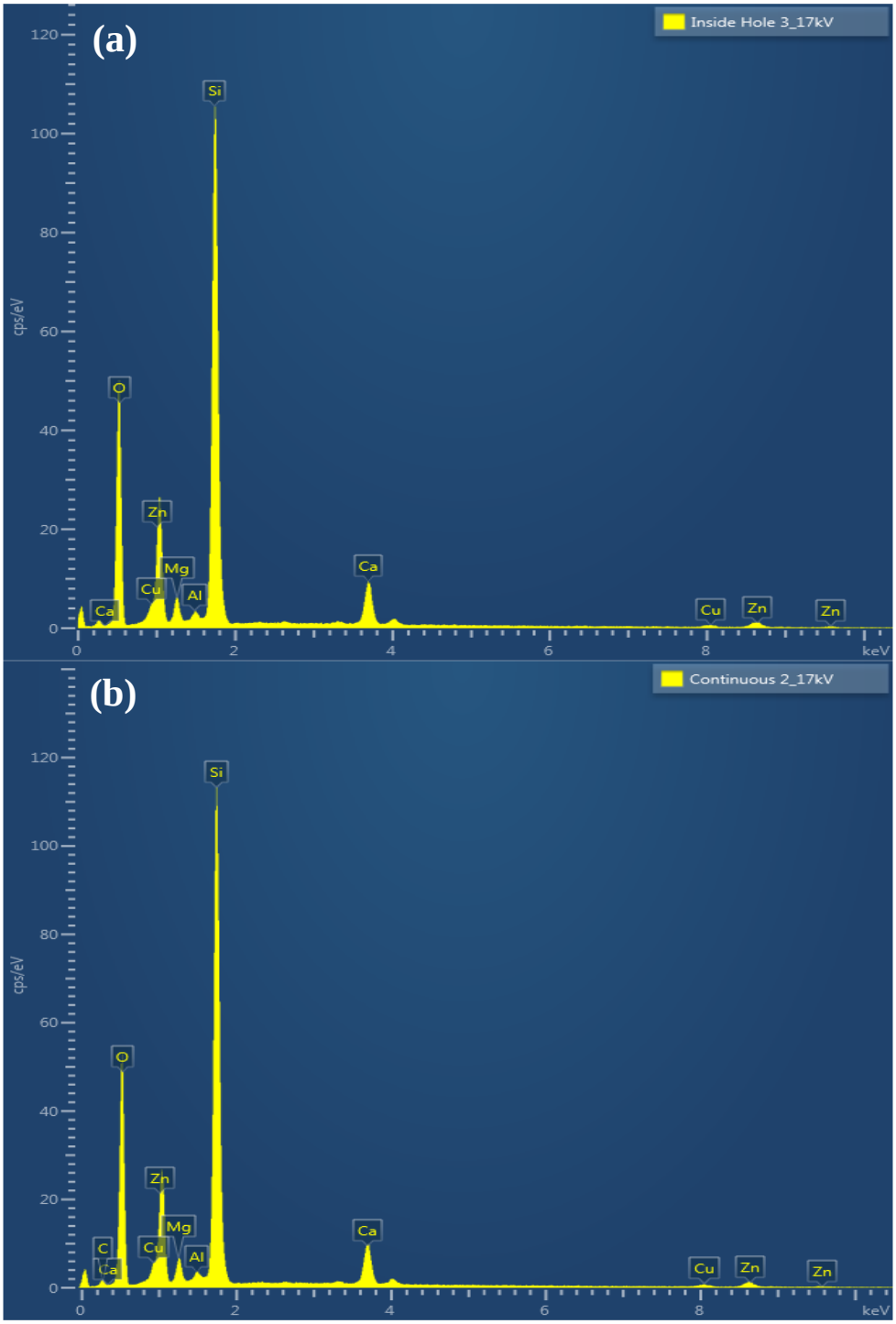

Figure S6: Representative EDXS spectra of nano-aperture Cu films with ZnO annealed at 180 ºC on glass substrates showing the distribution of elements **(a)** inside a hole and **(b)** in a continuous area.

Sample	O	Mg	Al	Si	Ca	Cu	Zn
Inside Hole	49.14	2.62	0.58	35.94	4.90	1.43	5.38
Continuous Area	43.90	2.45	0.51	38.2	5.82	3.70	5.43

Table S3: Representative elemental composition from EDXS spectra of nano-aperture Cu films with ZnO annealed at 180 ^{o}C on glass substrates showing the distribution of elements **(a)** inside a hole and **(b)** in a continuous area.

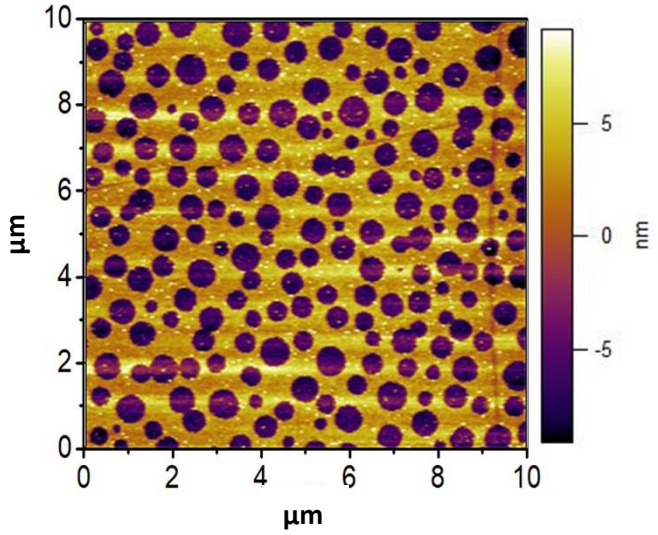

Figure S7: AFM image of a copper electrode (11 nm) which has been stored in the glove box for 5 months prior to removal of the ZnO overlayer using glacial acetic acid. The presence of apertures is evidence that the ZnO has been completely removed.

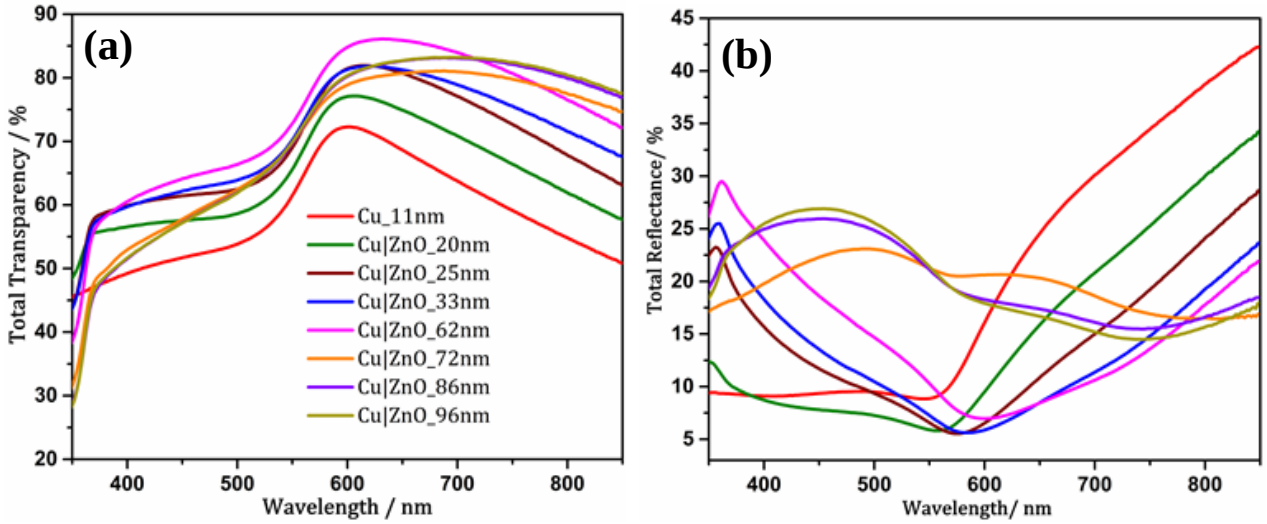

Figure S8: (a) Total far-field transparency and **(b)** reflectance of different thicknesses of ZnO spin cast on 11 nm thick planar Cu films.

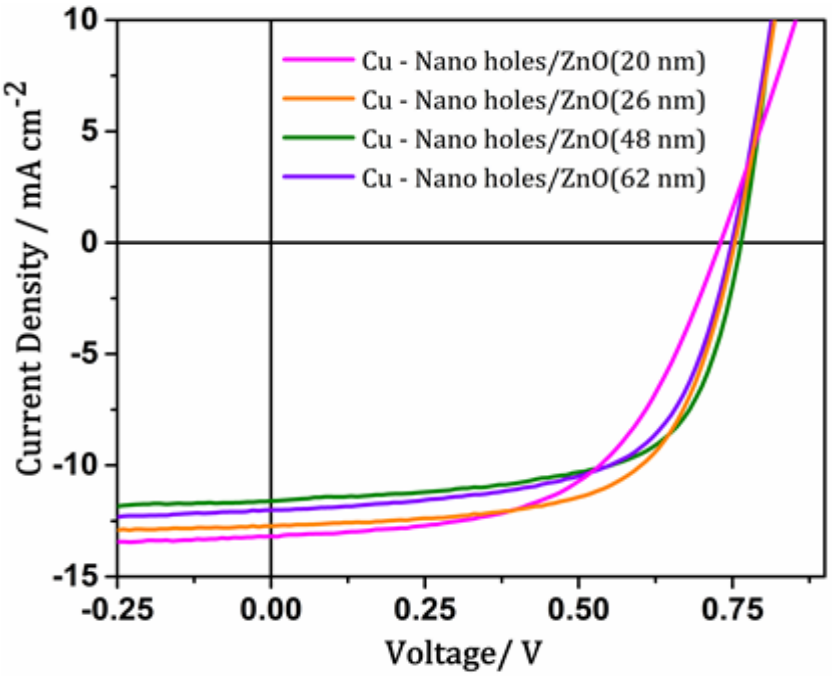

Figure S9: Representative current density – voltage characteristics under one sun simulated solar illumination (100 mW cm^{-2}; AM 1.5G) for devices with the

architecture: Cu (11nm) with nano holes / ZnO (X nm) / PEI (2 nm) / PCE10 – $PC_{70}BM$ (160 nm) / MoO_3 (10 nm)/ Ag (80 nm) for different thicknesses of ZnO.

Sample	J_{sc}/mA cm^{-2}	V_{oc}/ V	FF	R_s/ Ω cm^2	R_{shunt}/ Ω cm^2	PCE/ %
Cu – Planar / ZnO (33 nm)	9.58 ± 0.18	0.74 ± 0.01	0.68 ± 0.01	6.0 ± 0.5	1420 ± 65	4.77 ± 0.12
Champion	*9.73*	*0.74*	*0.68*			*4.93*
Cu - Nano holes/ ZnO (20 nm)	13.17 ± 0.15	0.73 ± 0.01	0.58 ± 0.03	14.1 ± 0.7	662 ± 55	5.66 ± 0.30
Champion	*13.37*	*0.75*	*0.60*			*6.00*
Cu - Nano holes/ ZnO (26 nm)	12.78 ± 0.27	0.76 ± 0.01	0.64 ± 0.02	8.1 ± 0.5	772 ± 47	6.18 ± 0.14
Champion	*12.76*	*0.76*	*0.66*			*6.44*
Cu - Nano holes/ ZnO (33 nm)	12.90 ± 0.46	0.76 ± 0.01	0.66 ± 0.01	6.1 ± 0.3	820 ± 52	6.47 ± 0.27
Champion	*13.51*	*0.76*	*0.67*			*6.80*
Cu - Nano holes/ ZnO (48 nm)	11.64 ± 0.17	0.76 ± 0.01	0.64 ± 0.02	7.9 ± 0.7	680 ± 63	5.64 ± 0.16
Champion	*11.87*	*0.76*	*0.66*			*5.90*
Cu - Nano holes/ ZnO (62 nm)	11.98 ± 0.08	0.75 ± 0.01	0.61 ± 0.01	8.7 ± 0.5	666 ± 36	5.47 ± 0.06
Champion	*12.00*	*0.75*	*0.62*			*5.57*
ITO/ ZnO (62 nm)	16.14 ± 0.13	0.72 ± 0.01	0.69 ± 0.01	7.3 ± 0.6	722 ± 38	8.04 ± 0.03
Champion	*16.40*	*0.72*	*0.69*			*8.15*

Table S4: Summary of current density - voltage characteristics of devices with the architecture; Cu (11nm)/ ZnO (x nm)/ PEI (2 nm) / PCE10 – $PC_{70}BM$ (160 nm) / MoO_3 (10 nm) / Ag (80 nm) where x = 20 - 62 nm tested under 1 sun

simulated solar illumination. The error bars represent ± 1 standard deviation determined from the performance of 20-30 devices with identical architecture.

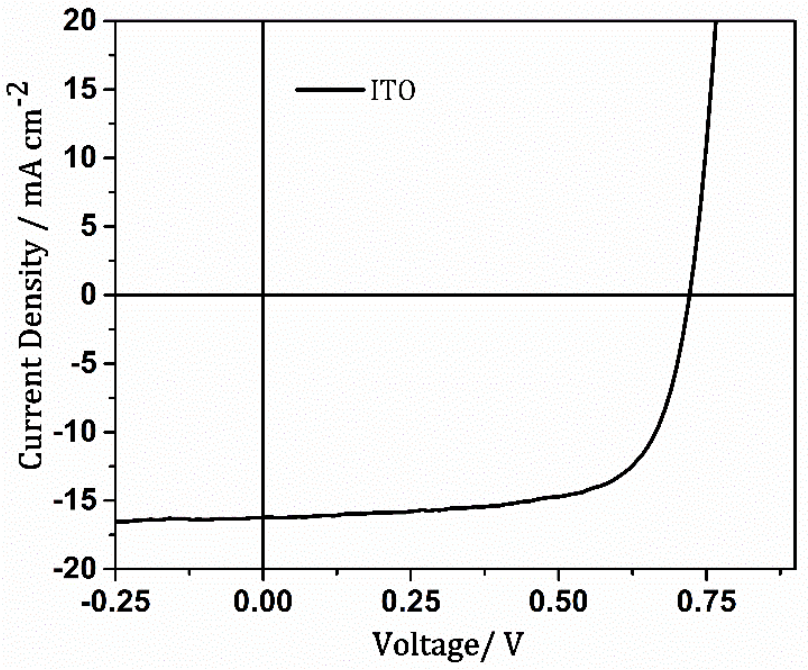

Figure S10: Representative current density – voltage characteristics under one sun simulated solar illumination (100 mW cm^{-2}; AM 1.5G) for devices with the architecture: ITO /ZnO (33 nm)/ PEI (2 nm) / PCE10 – $PC_{70}BM$ (160 nm) /MoO_3 (10 nm)/ Ag (80 nm).

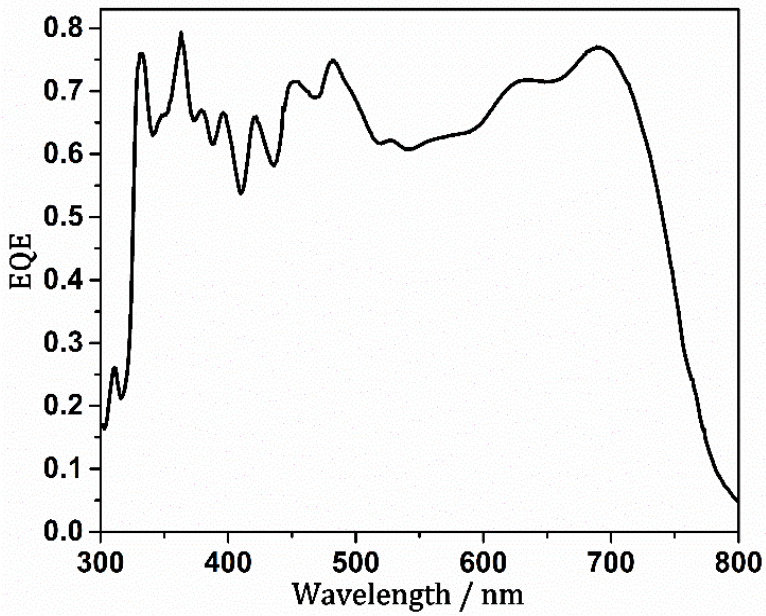

Figure S11: Representative EQE for devices with the architecture: ITO /ZnO (33 nm)/ PEI (2 nm) / PCE10 – $PC_{70}BM$ (160 nm) /MoO_3 (10 nm)/ Ag (80 nm).